Received: 26 April 2023 | Revised: 21 August 2023 | Accepted: 1 September 2023

DOI: 10.1002/nag.3625

RESEARCH ARTICLE

WILEY

Modelling seasonal landslide motion: Does it only depend on fluctuations in normal effective stress?

Fabio Rollo[1] | **Giuseppe Buscarnera**[2]

[1]Department of Structural and Geotechnical Engineering, Sapienza Università di Roma, Roma, Italy

[2]Department of Civil and Environmental Engineering, Northwestern University, Evanston, Illinois, USA

Correspondence
Fabio Rollo, Department of Structural and Geotechnical Engineering, Sapienza Università di Roma, via Eudossiana 18, 00184 Roma, Italy.
Email: fabio.rollo@uniroma1.it

Funding information
Italian Recovery and Resilience Plan; Integrative and Collaborative Education and Research, Grant/Award Number: 1854951

Abstract

Landslide motion is often simulated with interface-like laws able to capture changes in frictional strength caused by the growth of the pore water pressure and the consequent reduction of the effective stress normal to the plane of sliding. Here it is argued that, although often neglected, the evolution of all the 3D stress components within the basal shear zone of landslides also contributes to changes in frictional strength and must be accounted for to predict changes in seasonal velocity. For this purpose, an augmented sliding-consolidation model is proposed which allows for the computation of excess pore pressure development and downslope sliding with any constitutive law with 3D stress evolution. Simulations of idealised infinite slope models subjected to hydrologic forcing are used to study the role of in-situ stress conditions and stress rate multiaxiality. Specifically, a Drucker-Prager perfectly plastic model is used to replicate frictional failure and shear deformation at the base of landslides. The model reveals that conditions amenable to the shearing of a frictional interface are met only after numerous rainfall cycles, that is, when multiaxial stress rates are suppressed. In this case, the landslide is predicted to move through a seasonal ratcheting controlled only by the effective stress component normal to the plane of sliding. By contrast, in newly formed landslides, the multiaxial stress evolution is found to produce further regimes of motion, from plastic shakedown to cyclic failure, neither of which can be captured by interface-like frictional laws. Notably, the model suggests that a transition across these regimes can emerge in response to an aggravation of the magnitude of forcing, implying that (i) fluctuations in climate may alter the seasonal trends of motion observed today; (ii) our ability to quantify landslide-induced risks is impaired unless proper geomechanical models are used to examine their long-term dynamics.

KEYWORDS
constitutive modelling, hydro-mechanical coupling, rainfall-induced landslides, slope deformation

1 | INTRODUCTION

Rainfall is a primary factor in the modification of the hydro-mechanical regime within the ground and the mobilization of landslides, for example,[1,2] In the last decades, the risks posed by landslides have been aggravated by the emergence of alterations in global climate, with recent projections suggesting that an increase in the frequency and magnitude of landslides can be expected in several regions of the world, with obvious detrimental consequences for infrastructure and communities.[3] These concerns apply to landslides of all kinds, from translational earth slides involving shallow deposits (e.g.,[4–6]) to deeper deformation mechanisms typical of clay-rich formations (e.g.,[7–9].)

The increasing need of predicting current and future landslide risks has inspired a growing body of literature emphasising the link between pore water pressure rise and landslide motion. Notable examples are numerical analyses based on the Finite Element Method (FEM) (e.g.,[10–13]) as well as techniques such as the Material Point Method (MPM) (e.g.,[14–16]) and Smoothed Particle Hydrodynamics (SPH) (e.g.,[17–19]) which provide benefits for the study of high mobility events. In these methods, coupled hydro-mechanical formulations enable the quantification of landslide displacements as an outcome of pore pressure increase and soil strength deterioration. However, their computational cost often poses limitations to a unified assessment of the pre- and post-failure motion of landslides over long periods of time, as is necessary to tackle climate effects changing over multiple years, or even decades.

To overcome these obstacles, interesting alternatives are offered by semi-analytical approaches focusing on simplified slope geometries and materials models, but also able to capture the coupling between hydraulic and mechanical processes with closed-form analytical solutions and/or low-cost numerical integration. A notable example is the sliding-consolidation model proposed by Hutchinson,[20] originally designed to capture the runout of shallow landslides undergoing liquefaction. By using the scheme of infinite slope, this model captures the role of consolidation in modulating the frictional strength at the base of a moving landslide mass. The simplicity of the formulation offered opportunities for subsequent extensions aimed at capturing the movement of mobilized soil volumes either by allowing for changes in the geometry of the mass through depth-integrated formulations and simple rheological laws[21,22] or by taking into account the topographic features of the terrain.[23] Similar developments carried out by Iverson[24] for more general slope deformation processes enabled a closed-form consideration of the coupling between landslide motion and pore pressure development, thus opening the way for an integrated analysis of triggering and deformation. However, this model was restricted to a perfectly plastic frictional response of the basal shear zone and a constant diffusion coefficient that ignored how pore pressure development can be affected by inelastic deformation. Such shortcomings have been recently removed by an enhanced framework proposed by Chen and Buscarnera,[25] where the hydro-mechanical feedbacks at the base of a landslide are treated with explicitly defined constitutive laws, thus allowing for a timescale of pore pressure diffusion regulated by the rate of soil strength deterioration. Such unique features have recently enabled the coupling between pore pressure development/dissipation in the shear zone and rainfall infiltration, thus capturing hydrologically-driven landslide motion as a direct outcome of the shear zone rheology.[26] Despite the versatility of this new framework, demands of analytical simplicity and consistency with prior sliding consolidation models led Chen and Buscarnera[25] to adopt a constitutive law resolving only shear and normal effective stress components at the base of a translational landslide (e.g.,[27]). This choice is referred to as *interface-like* modelling of the basal shear zone behaviour.

This paper examines the implications of this common approximation for the deformation of the shear zone, in an attempt to address the following question: does the evolution of 3D stress components in the basal shear zone of a landslide affect the hydro-mechanics of landslides and, thus, their seasonal regime of motion? To answer this question, a further enhancement of the framework proposed by Chen and Buscarnera[25] is proposed, which relies on the incorporation of constitutive laws with no restrictions on the dimensionality of stress state representation. This idea is consistent with previous works that reported how the stress components laying within the plane of sliding (i.e., along the downslope and out-of-plane directions) affect the shearing of frictional materials.[28–30] At variance with earlier studies, however, the analyses conducted here emphasise how such constitutive effects interact with water infiltration. The goal is to identify the scenarios, if any, in which multiaxial stress rate evolution is negligible, as well as those requiring its explicit consideration. In the following, the key steps to incorporate the full 3D stress state evolution into the sliding-consolidation model proposed by Chen and Buscarnera[25] are discussed. Then, selected simple shear simulations are conducted to show how pseudo-hardening and pseudo-softening effects documented in previous studies (e.g.,[29,31]) interact with rainfall-induced pore pressures. For this purpose, a perfectly plastic Drucker-Prager constitutive law with a non-associated flow is used to examine the role of evolving 3D stress state in shear deformation at the base of a landslide. Finally, the performance of the augmented framework is illustrated with reference to simulations of moving translational landslides. While the

examples are inspired by field-scale observations, their goal is to highlight in general terms the effect of rainfall cycles on the landslide dynamics, explaining how variations in the magnitude of hydrologic forcing affect their seasonal response.

2 | INCORPORATION OF MULTIAXIAL CONSTITUTIVE BEHAVIOUR INTO A SLIDING-CONSOLIDATION MODEL

The sliding consolidation model presented here aims at describing coupled transient pore pressure evolution and downslope motion dynamics beneath a landslide mass subjected to hydrologic forcing. The analysis is conducted with reference to infinite slopes of given inclination (here quantified by the slope angle α, in Figure 1). Inelastic deformation and excess pore pressure development are assumed to be confined in a shear band of thickness h_s, while the overlaying material is treated as a saturated rigid block that: (i) affects the state of stress at the base of the deformable layer through its weight; (ii) allows pore water diffusion and pressure changes in response to rainfall inputs; (iii) serves as a drainage zone for the water held within the basal shear zone of the landslide. Although the framework allows for an explicit link to linear or nonlinear rainfall infiltration models,[26] here a simpler approach is used, according to which the diffusion analysis in the upper block is by-passed and replaced by a pore pressure input at the top of the basal shear zone, which effectively models the hydrologic forcing driving effective stress change and shear strains beneath the landslide. By contrast, the bedrock in contact with the bottom of the shear zone is modelled as an impervious contour. As such, this simplified scheme leads to a one-dimensional problem in which only the downslope acceleration (axis η) and the fluid diffusion in the vertical direction (axis z) are taken into account.

The initial pore pressure profile at time t_0 represents the static pore water pressure, p_w^s, prior to a rainfall event and depends on the position of the ground water level (h_w), while the dashed line in Figure 1 denotes the shifted profile of pore water pressure caused at time t_1 by rainfall infiltration. The evolution of the pore pressure $p_w(t)$ within the basal shear zone is governed by the consolidation process and is represented in terms of isochrones. After the triggering of downslope motion, and thus the emergence of permanent strains, the temporal dynamics of such isochrones are regulated by the plastic properties of the soil in the basal process zone, and hence by the selected constitutive law. The pore pressure change at the top of the shear zone, $\Delta p_w^t(t)$, reflects the prescribed hydrologic forcing in response to rainfall, while $p_w^b(t) = p_w^{sb} + p_w^{eb}(t)$ is the basal pore pressure[24] sum of the static and the excess pore pressure, $p_w^{eb}(t)$, that evolves as a function of coupled hydro-mechanical processes regulated by inelastic deformation. In the following, the soil mechanics sign convention (compressive positive) is assumed, and the effective stresses are denoted with σ'. The engineering (i.e., Voigt) notation is used for stress and strain, with σ, τ and ε, γ denoting normal and shear stresses and strains, respectively. Compared to Chen and Buscarnera,[25] the use of a 3D constitutive formulation adopted in this work requires explicit enforcement of plane strain conditions, with $\dot{\varepsilon}_\chi = \dot{\gamma}_{\chi\xi} = \dot{\gamma}_{\chi\eta} = 0$ as the displacement along the out of plane axis χ is zero, and $\dot{\varepsilon}_\eta = 0$ as the slope is infinitely extended. Therefore, the constitutive behaviour is described considering the state of

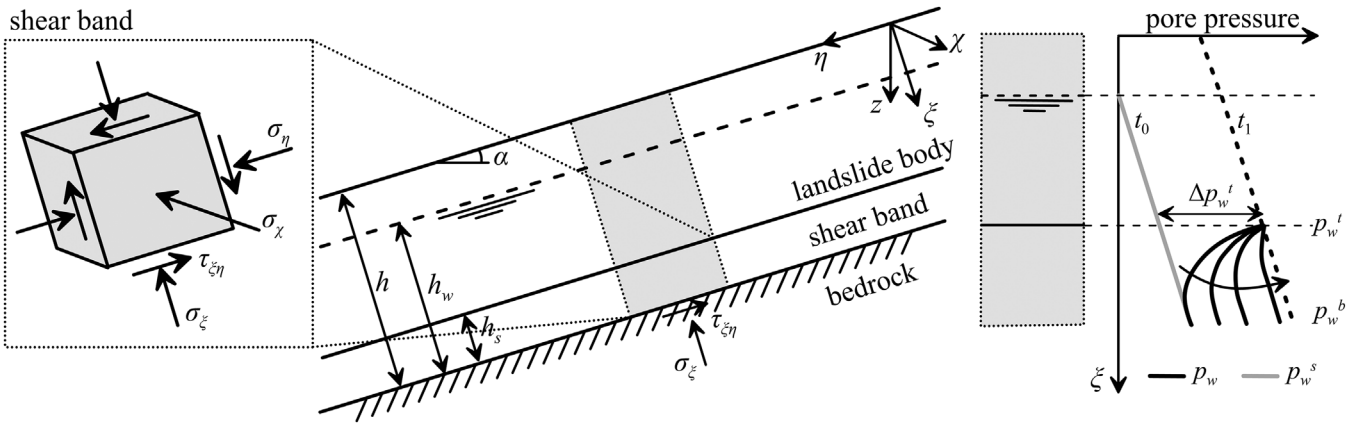

FIGURE 1 Infinite slope subjected to excess pore pressure evolution at its base. The insert on the left indicates the stress components affecting simple shear deformation, while sketches of pore pressure profiles shifting during rainfall are provided on the right. A dashed line indicates a shifted pore pressure profile at a selected time during rainfall. The arrow indicates the trend of evolution of the pore pressure profiles due to the ongoing consolidation from time t_0 to t_1, regulated by the inelasticity of the basal shear zone after triggering.

stress within the shear zone represented in Figure 1, with the shear stresses $\tau_{\xi\chi} = \tau_{\chi\eta} = 0$ because of the symmetry of the problem, σ_ξ the normal stress to the slip surface, σ_η the downslope stress component, σ_χ the out-of-plane principal stress and $\tau_{\xi\eta}$ the shear stress acting at the base. According to the principle of effective stresses one can write

$$\dot{p}_w = \dot{\sigma}_{\xi,d} - \dot{\sigma}'_\xi \tag{1}$$

where $\sigma_{\xi,d}$ is the driving total normal stress and the prime denotes the effective stress. Moreover, the Newton's law in the direction parallel to the slope surface leads to

$$\rho h \ddot{v} = \dot{\tau}_{\xi\eta,d} - \dot{\tau}_{\xi\eta,f} \tag{2}$$

where $\tau_{\xi\eta,d}$ is the driving shear stress due to external loading, $\tau_{\xi\eta,f}$ the soil shear strength, $\dot{v} = a$ the downslope acceleration, h the total thickness of the soil column and ρ the equivalent density. Under the assumption of fluid incompressibility,[32,33] the vertical fluid diffusion is expressed via the partial differential equation

$$\frac{\partial q_z}{\partial z} + \dot{n} = 0 \tag{3}$$

with n the porosity and q_z the vertical water flux. Recalling the Darcy's law and that for small strain theory[34] is $\dot{n} = -\dot{\varepsilon}_\xi$, Equation (3) can be rewritten as

$$\frac{k}{\gamma_w}\frac{\partial^2 p_w}{\partial z^2} + \dot{\varepsilon}_\xi = 0 \tag{4}$$

where k is the hydraulic conductivity, γ_w the unit weight of the water and ε_ξ the strain component normal to the slip surface.

By virtue of the hypothesis of additive decomposition of elastic and plastic strain tensors, $\boldsymbol{\varepsilon} = \boldsymbol{\varepsilon}^e + \boldsymbol{\varepsilon}^p$, the constitutive relationship can be expressed as

$$\begin{Bmatrix} \dot{\sigma}'_\xi \\ \dot{\sigma}'_\eta \\ \dot{\sigma}'_\chi \\ \dot{\tau}_{\xi\eta} \end{Bmatrix} = \begin{bmatrix} D^e_{11} & D^e_{12} & D^e_{13} & D^e_{14} \\ D^e_{21} & D^e_{22} & D^e_{23} & D^e_{24} \\ D^e_{31} & D^e_{32} & D^e_{33} & D^e_{34} \\ D^e_{41} & D^e_{42} & D^e_{43} & D^e_{44} \end{bmatrix} \begin{Bmatrix} \dot{\varepsilon}^e_\xi \\ \dot{\varepsilon}^e_\eta \\ \dot{\varepsilon}^e_\chi \\ \dot{\gamma}^e_{\xi\eta} \end{Bmatrix} \tag{5}$$

where D^e_{ij} represents the elastic stiffness matrix. Combining Equations (1)-(5) and the relationship between the shear strain rate and the gradient of the flow velocity $\dot{\gamma}_{\xi\eta} = -\partial v(\xi)/\partial\xi$, the governing equations of the dynamic hydro-mechanical coupled model become

$$\begin{aligned} \dot{p}_w &= \frac{D^e_{11} k}{\gamma_w}\frac{\partial^2 p_w}{\partial \xi^2} + D^e_{11}\dot{\varepsilon}^p_\xi + \dot{\sigma}_{\xi,d} + D^e_{14}\left(\frac{\partial v}{\partial \xi} + \dot{\gamma}^p_{\xi\eta}\right) + D^e_{12}\dot{\varepsilon}^p_\eta + D^e_{13}\dot{\varepsilon}^p_\chi \\ \rho h \ddot{v} &= \dot{\tau}_{\xi\eta,d} + D^e_{44}\left(\frac{\partial v}{\partial \xi} + \dot{\gamma}^p_{\xi\eta}\right) + \frac{D^e_{41} k}{\gamma_w}\frac{\partial^2 p_w}{\partial \xi^2} + D^e_{41}\dot{\varepsilon}^p_\xi + D^e_{42}\dot{\varepsilon}^p_\eta + D^e_{43}\dot{\varepsilon}^p_\chi \end{aligned} \tag{6}$$

Following Chen and Buscarnera,[25] two analytical simplifications are introduced for the pore water pressure distribution and the velocity field within the shear band. Specifically, the profile of the excess pore pressure is represented by a parabolic function,[35] with $\Delta p^t_w(t)$ denoting the pore water pressure change at the top due to rainfall infiltration and derivative $\mathrm{d}p^e_w/\mathrm{d}z = 0$ at $z = h_s \cos\alpha$ to simulate the impervious interface

$$p^e_w(z) = -\frac{p^{eb}_w - \Delta p^t_w}{(h_s \cos\alpha)^2} z^2 + 2\frac{p^{eb}_w - \Delta p^t_w}{h_s \cos\alpha} z + \Delta p^t_w \tag{7}$$

Similarly, the profile of the flow velocity within the shear zone is assumed linear with zero velocity at the bottom of the layer, leading to

$$v = v_t \left(1 - \frac{\xi}{h_s}\right) \tag{8}$$

where v_t denotes the flow velocity at the top of the shear zone. Therefore, the total normal strain rate to the slope surface and the shear strain rate become

$$\dot{\varepsilon}_\xi = \frac{2k}{\gamma_w h_s^2 \cos^2\alpha}\left(p_w^{eb} - \Delta p_w^t\right) \qquad \dot{\gamma}_{\xi\eta} = -\frac{\partial v}{\partial \xi} = \frac{v_t}{h_s} \tag{9}$$

These simplifications allow to reformulate the partial differential equations of Equation (6) as a system of coupled ordinary differential equations, as follows

$$\begin{aligned}
\dot{p}_w^{eb} &= \underbrace{-\frac{2D_{11}^e k}{\gamma_w h_s^2 \cos^2\alpha}\left(p_w^{eb} - \Delta p_w^t\right) + D_{11}^e \dot{\varepsilon}_\xi^p + \dot{\sigma}_{\xi,d}}_{\text{interface-like terms}} \underbrace{-\frac{D_{14}^e}{h_s} v_t + D_{14}^e \dot{\gamma}_{\xi\eta}^p + D_{12}^e \dot{\varepsilon}_\eta^p + D_{13}^e \dot{\varepsilon}_\chi^p}_{\text{multiaxial terms}} \\
\rho h \ddot{v}_t &= \underbrace{\dot{\tau}_{\xi\eta,d} - \frac{D_{44}^e}{h_s} v_t + D_{44}^e \dot{\gamma}_{\xi\eta}^p}_{\text{interface-like terms}} \underbrace{-\frac{2D_{41}^e k}{\gamma_w h_s^2 \cos^2\alpha}\left(p_w^{eb} - \Delta p_w^t\right) + D_{41}^e \dot{\varepsilon}_\xi^p + D_{42}^e \dot{\varepsilon}_\eta^p + D_{43}^e \dot{\varepsilon}_\chi^p}_{\text{multiaxial terms}}
\end{aligned} \tag{10}$$

in which the plastic behaviour as well as the elastic stiffness components depend on the selected constitutive law. The equations above generalise those obtained by Chen and Buscarnera[25] with reference to an interface-like $\sigma' - \tau$ formulation, in that they encompass additional terms emerging from multiaxial effects. Specifically, the pore water pressure beneath the landslide also depends on the downslope ($\dot{\varepsilon}_\eta^p$) and out-of-plane ($\dot{\varepsilon}_\chi^p$) plastic strain rates by virtue of the stiffness components D_{12}^e and D_{13}^e. Moreover, when accounting for elastic nonlinearity and/or anisotropy (e.g.,[36]) terms D_{14}^e, D_{24}^e and D_{34}^e appear, leading to further volumetric-deviatoric couplings. It can be thus concluded that a 3D constitutive framework recovers the interface-like response as a particular case when the abovementioned terms vanish or become negligible. In the following, the conditions under which such simplifications are acceptable, if any, will be pointed out.

In summary, compared to an interface-like ($\sigma' - \tau$) model, the use of a 3D formulation leads to eight new terms in Equation (10). According to classical elasto-plasticity, and by denoting the plastic potential function with g, the plastic strain rates are given by $\dot{\boldsymbol{\varepsilon}}^p = \Lambda \partial g / \partial \boldsymbol{\sigma}'$. The plastic multiplier, Λ, can be obtained by imposing the consistency condition to the yield function f, which for the problem under study takes the following form:

$$\Lambda = \frac{\frac{\partial f}{\partial \boldsymbol{\sigma}'}^T \mathbb{D}^e \dot{\boldsymbol{\varepsilon}}}{-\frac{\partial f}{\partial \mathbf{q}} : \mathbf{h} + \frac{\partial f}{\partial \boldsymbol{\sigma}'} \mathbb{D}^e \frac{\partial g}{\partial \boldsymbol{\sigma}'}} = \frac{B_1 \dot{\varepsilon}_\xi + B_2 \dot{\gamma}_{\xi\eta}}{H - H_c} = \frac{B_1 \frac{2k}{\gamma_w h_s^2 \cos^2\vartheta}\left(p_w^{eb} - \Delta p_w^t\right) + B_2 \frac{v_t}{h_s}}{H - H_c} \tag{11}$$

where $\mathbb{D}^e$ is the fourth-order elastic stiffness tensor, H and H_c are the hardening and critical hardening moduli, $\mathbf{q}$ is the vector of internal variables, $\mathbf{h}$ the hardening function, and the scalar values B_1 and B_2 are defined as

$$\begin{aligned}
B_1 &= \frac{\partial f}{\partial \sigma'_\xi} D_{11}^e + \frac{\partial f}{\partial \sigma'_\eta} D_{21}^e + \frac{\partial f}{\partial \sigma'_\chi} D_{31}^e + \frac{\partial f}{\partial \tau_{\xi\eta}} D_{41}^e \\
B_2 &= \frac{\partial f}{\partial \sigma'_\xi} D_{14}^e + \frac{\partial f}{\partial \sigma'_\eta} D_{24}^e + \frac{\partial f}{\partial \sigma'_\chi} D_{34}^e + \frac{\partial f}{\partial \tau_{\xi\eta}} D_{44}^e
\end{aligned} \tag{12}$$

Combining the flow rule, Equation (10) and the right-side term of Equation (11), the governing equations assume the form

$$\begin{aligned}
\dot{p}_w^{eb} &= \frac{2k}{\gamma_w h_s^2 \cos^2\alpha}\left(\frac{B_1 B_3}{H - H_c} - D_{11}^e\right)\left(p_w^{eb} - \Delta p_w^t\right) + \left(\frac{B_2 B_3}{H - H_c} - D_{14}^e\right)\frac{v_t}{h_s} + \dot{\sigma}_{\xi,d} \\
\rho h \ddot{v}_t &= \dot{\tau}_{\xi\eta,d} + \frac{2k}{\gamma_w h_s^2 \cos^2\alpha}\left(\frac{B_1 B_4}{H - H_c} - D_{41}^e\right)\left(p_w^{eb} - \Delta p_w^t\right) + \left(\frac{B_2 B_4}{H - H_c} - D_{44}^e\right)\frac{v_t}{h_s}
\end{aligned} \tag{13}$$

with the terms B_3 and B_4 expressed as

$$\begin{aligned} B_3 &= D^e_{11}\frac{\partial g}{\partial \sigma'_\xi} + D^e_{12}\frac{\partial g}{\partial \sigma'_\eta} + D^e_{13}\frac{\partial g}{\partial \sigma'_\chi} + D^e_{14}\frac{\partial g}{\partial \tau_{\xi\eta}} \\ B_4 &= D^e_{41}\frac{\partial g}{\partial \sigma'_\xi} + D^e_{42}\frac{\partial g}{\partial \sigma'_\eta} + D^e_{43}\frac{\partial g}{\partial \sigma'_\chi} + D^e_{44}\frac{\partial g}{\partial \tau_{\xi\eta}} \end{aligned} \tag{14}$$

Finally, the governing equations can be rewritten in the form

$$\begin{Bmatrix} \dot{p}^{eb}_w \\ \dot{v}_t \\ \dot{a} \end{Bmatrix} = \begin{bmatrix} A_{11} & A_{12} & 0 \\ 0 & 0 & 1 \\ A_{21} & A_{22} & 0 \end{bmatrix} \begin{Bmatrix} p^{eb}_w - \Delta p^t_w \\ v_t \\ a \end{Bmatrix} + \begin{Bmatrix} \dot{\sigma}_{\xi,d} \\ 0 \\ \dot{\tau}_{\xi\eta,d}/\rho h \end{Bmatrix} \tag{15}$$

With the coefficients of matrix **A,** expressed as

$$\begin{aligned} A_{11} &= \frac{2k}{\gamma_w h_s^2 \cos^2\alpha}\left[\frac{B_1 B_3}{H - H_c} - D^e_{11}\right] \\ A_{12} &= \frac{1}{h_s}\left(\frac{B_2 B_3}{H - H_c} - D^e_{14}\right) \\ A_{21} &= \frac{2k}{\gamma_w h_s^2 \cos^2\alpha}\left[\frac{B_1 B_4}{H - H_c} - D^e_{41}\right] \\ A_{22} &= \frac{1}{h_s}\left(\frac{B_2 B_4}{H - H_c} - D^e_{44}\right) \end{aligned} \tag{16}$$

The components of matrix **A** reflect the temporal dynamics of the landslide response, which depends on the deformation behaviour within the shear zone and can be specialised to any constitutive law.

3 | ROLE OF THE STRESS MULTIAXIALITY UNDER SIMPLE SHEAR CONDITIONS

Here a specific linear elastic perfectly plastic constitutive law is used to illustrate how multiaxial stress evolution affects shearing beneath a landslide. Such class of models is widely used in landslide applications, in that frictional criteria represent the baseline to interpret evidence and constrain the properties of site-specific soils. Although the Mohr-Coulomb (MC) model is a widely used standard, here, the Drucker-Prager (DP) model is selected for analyses. This choice is primarily justified by arguments of mathematical simplicity, in that the lack of Lode angle dependence characterising the DP model leads to a more compact description of 3D stress evolution, without loss of generality for the key conceptual points regarding stress multiaxiality. In addition, proper calibration of the DP model parameters involves minor quantitative differences compared to the results that would be obtained from the use of the MC model, up to the point of making the difference between the two nearly negligible for practical considerations.

The yield function is therefore defined conveniently in terms of stress invariants, as

$$f = \frac{q}{\sqrt{3}}K_f(\vartheta) - p'\sin\varphi - c\cos\varphi = 0\,,\; K_f(\vartheta) = \cos\vartheta - \frac{\sin\vartheta\sin\varphi}{\sqrt{3}} \tag{17}$$

where $p' = 1/3\mathrm{tr}(\boldsymbol{\sigma}') = 1/3\sigma'_{ii}$ is the mean effective pressure, $q = \sqrt{3/2\mathbf{s} : \mathbf{s}}$ the deviatoric stress, $\mathbf{s}$ the deviatoric stress tensor, ϑ the Lode angle, c the cohesion, and φ the friction angle. The function $K_f(\vartheta)$ controls the size of the yield surface and its dependence on ϑ is constant for the Drucker-Prager model. The plastic potential function g depends on the dilatancy angle ψ that governs the non-associativeness of flow rule, as follows:

$$g = \frac{q}{\sqrt{3}}K_g(\vartheta) - p'\sin\psi - c\cos\psi = 0, \quad K_g(\vartheta) = \cos\vartheta - \frac{\sin\vartheta\sin\psi}{\sqrt{3}} \tag{18}$$

For quasi-saturated ground conditions, it is reasonable to assume that during the process of water infiltration the landslide shear zone undergoes changes in stress driven by the pore pressure increase (e.g., reduction in normal effective stress, σ'_ξ) under nearly constant downslope shear stress, $\tau_{\xi\eta}$. Simple shear simulations are thus performed here to shed light on how this process leads to inelastic deformation and, possibly, strength loss. Specifically, we seek to emphasise how 3D stress evolution mediated by the initial state of stress prior to rainfall controls the inelastic deformation. To this purpose, the Drucker-Prager model was calibrated to obtain the same strength of the Mohr Coulomb under pure shear conditions ($\vartheta = 0°$), as illustrated in the normalised deviatoric plane of Figure 2, where s_1, s_2 and s_3 are the principal deviatoric stresses. As such, the response of Drucker-Prager model is comparable to that of the Mohr Coulomb for $-30° < \vartheta < 0°$, while it underestimates the strength under triaxial compression ($\vartheta = 30°$).

The drained simple shear response of a soil element is illustrated first, as it mimics the conditions of an infinite slope under shear perturbations. Elastic properties corresponding to shear modulus $G = 2000$ kPa and Poisson's ratio $\nu = 0.25$ are used, while for the inelastic response a purely frictional material is considered ($\varphi = 30°$; $c = 0$) with two distinct values of dilatancy angle (namely, $\psi = 30°$, corresponding to associated plastic flow, and $\psi = 0°$, corresponding to non-associated flow). The initialisation of the stress state is carried out by imposing different values of earth coefficient at rest, K_0, ensuring that the initial state lies within the yield surface (i.e., initially elastic conditions).

Figure 3 shows the results in terms of shear stress and volumetric strain plotted against the shear strain for the cases of associated and non-associated flow rule and for three values of $K_0 = 0.5, 1.0, 1.5$ reflecting different overconsolidation ratios of the soil, aimed at clarifying the effect of the initial effective stress. In detail, the normal stress component is $\sigma'_\xi = 100$kPa, the other components are $\sigma'_\eta = \sigma'_\chi = K_0\sigma'_\xi$ and, for the sake of clarity, zero initial shear stress is considered. Figure 3A and C shows the stress-strain curves and the volumetric strain $\varepsilon_v = \mathrm{tr}(\boldsymbol{\varepsilon}) = \varepsilon_{ii}$ obtained through the Drucker-Prager model. Although the model is elastic-perfectly plastic, in the presence of non-associated plastic flow the stress-strain curves display pseudo-hardening after first yielding, while softening is computed for $K_0 > 1$. First yielding conditions depend only on the initial stress state and are unaffected by the flow rule. By contrast, the strength at large deformation is found to depend on the choices made for the plastic flow rule (i.e., on the value of the dilation angle), regardless of the initial state of stress. The nonlinear behaviour observed upon first yielding arises as a natural consequence of the stress evolution due to the 3D constitutive relationship.

Although these features have been already pointed out by Vermeer[37] and di Prisco and Pisanò,[29] they are worth discussing in light of the augmented framework presented in the previous section. In fact, these trends underpin multiaxial stress effects embedded in the evolution of the terms B_1 and B_3 of Equation (12) and Equation (14) (Figure 3B-D), and thus exert a direct influence in the landslide dynamics, as reflected by the expression of the dynamic coefficients in Equations (15)-(16)-. Under specific stress state conditions, the response is elastic-perfectly plastic and coincides with that of an interface-like model, as in the case of $\psi = 0°$ and $K_0 = 1$. Except these limited cases, the terms B_1 and B_3 of Equation (12) and Equation (14) are not constant during the plastic regime, in that they evolve during the shearing process leading to a constitutive behaviour characterised by either pseudo-softening or pseudo-hardening. From a landslide mechanics standpoint, the evolution of these terms clearly alters the deformation dynamics embedded in Equation (15) and augments its nonlinearity. However, when the stress state reaches a steady-state condition and the multiaxial effects vanish, the

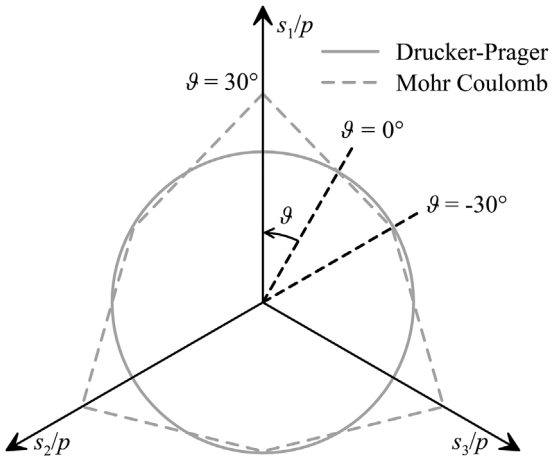

FIGURE 2 Yield surfaces plotted in the π-plane and geometric interpretation of the Lode angle, θ.

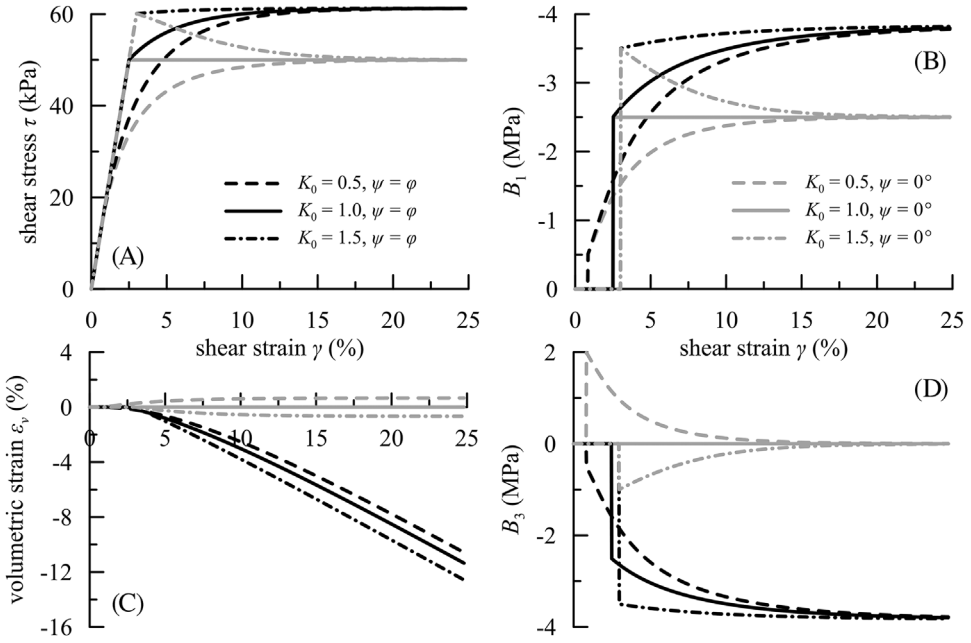

FIGURE 3 Simulations of drained simple shear tests for different initial stress states and for associated and non-associated flow rule: (A) stress-strain response; (B) volumetric deformation response; (C,D) scalar coefficients B_1 and B_3 controlling the effect of basal plastic deformation on the dynamics of a hydrologically-driven shallow landslide.

multiaxial formulation degenerates to an interface-like behaviour, with terms B_1 and B_3 assuming constant values. The interpretation of the results is further clarified by plotting the stress paths in the normalised deviatoric plane, as shown in Figure 4. The yield locus of the Mohr Coulomb model is also reported with dashed line for comparison. As long as the response is elastic the stress cartesian components along the three chosen axes are constant but, after first yielding, σ'_η and σ'_χ evolve and the stress path follows the yield locus tangentially (neutral loading) until a final stress state. In simple shear condition, the requirement $\dot{\sigma}'_\eta = \dot{\sigma}'_\chi = 0$ implies $\dot{\varepsilon}^p_\eta = \dot{\varepsilon}^p_\chi = 0$, that in combination with the consistency condition $f = 0$ leads to the following value of K_0:

$$K_0 = \frac{\left(\sqrt{3}\cos\vartheta - \sin\vartheta\sin\psi\right)\left(\sqrt{3}\cos\vartheta - \sin\vartheta\sin\varphi\right) + 2\sin\psi\sin\varphi}{\left(\sqrt{3}\cos\vartheta - \sin\vartheta\sin\psi big\right)\left(\sqrt{3}\cos\vartheta - \sin\vartheta\sin\varphi\right) - 4\sin\psi\sin\varphi} \tag{19}$$

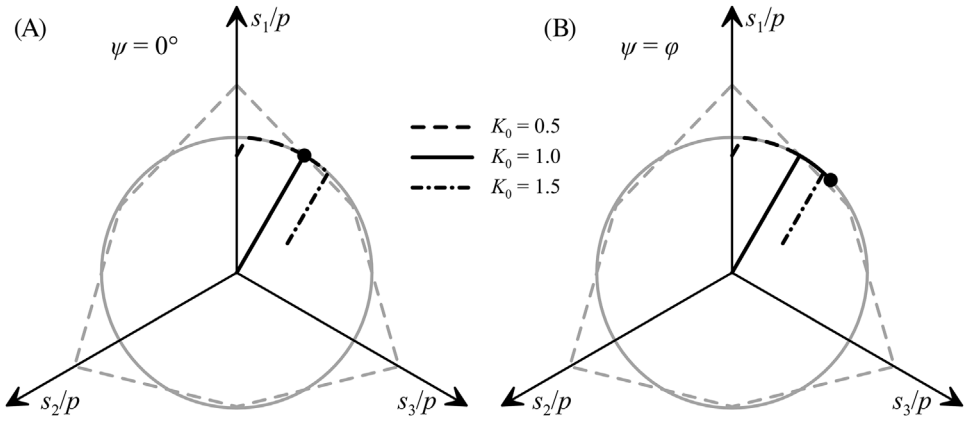

FIGURE 4 Stress paths in π-plane computed for drained simple shear tests simulated with a Drucker-Prager model for (A) $\psi = 0°$ and (B) $\psi = \varphi$ and different initial stress states. The dots indicate the stress states at ultimate conditions (i.e., achieved upon large shear strain).

From Equation (19) it is apparent that $\psi = 0°$ implies $\sigma'_\eta = \sigma'_\chi = \sigma'_\xi$ and the final stress state lies on the line at $\vartheta = 0°$. By contrast, for $\psi > 0°$ the stress state lies on the yield surface within the range $-30° < \vartheta < 0°$. The stress state at $\vartheta = -30°$ refers to triaxial extension (i.e., zero shear stress), thus impossible to attain during simple shear loading. The pseudo-hardening and softening obtained from the simulations can be properly justified considering the evolution of the cartesian stress components according to Equation (19). In fact, for initial states characterised by $K_0 < 1$ the downslope and out of plane stress components σ'_η and σ'_χ increase, with greater values of mean effective pressure that produces hardening, while for initial $K_0 > 1$ the reduction of mean effective pressure leads to softening. Moreover, the dilatancy plays a crucial role as tends to inhibit the tendency of the soil element to soften after first yielding and leads to higher values of the final strength.

To reproduce the stress path followed by a soil element within sloping ground during the process of water infiltration, a series of simulations of stress-controlled tests at constant shear stress have been performed. To simulate the reduction of effective stresses induced by the pore water pressure build-up, the normal stress σ'_ξ is gradually reduced while the shear stress $\tau_{\xi\eta}$ is kept constant. According to the scheme of infinite slope of Figure 1, the state of stress is initialised as

$$\begin{aligned} \sigma_\xi &= \gamma z \cos^2\alpha \\ \tau_{\xi\eta} &= \gamma z \sin\alpha \cos\alpha \\ \sigma'_\eta &= \sigma'_\chi = K_0 \sigma'_\xi \end{aligned} \tag{20}$$

where γ is the unit weight of the soil and α is the slope angle. The initial stress state is evaluated for dry conditions at a depth of $z = 10$m, with a unit weight $\gamma = 20\text{kN/m}^3$ and a slope angle $\alpha = 5°$ with earth coefficient at rest $K_0 = 0.5, 1.0, 1.5$. Figure 5 shows the results of the simulations in terms of (a) stress paths in the p'-q plane, (b) shear strain and (c) volumetric strain against the ratio $\tau_{\xi\eta}/\sigma'_\xi$ using the same model parameters adopted above and two values of dilatancy angle $\psi = 30°$ and $\psi = 0°$ to account for associated and non-associated flow, respectively.

At the beginning of the simulated test, when the response is elastic, the reduction of the normal stress σ'_ξ is accompanied by reduction of the mean effective pressure and dilative response; then, when first yielding is reached the stress state keeps moving along the yield criterion (Figure 5A) with evolution of the stress components σ'_η and σ'_χ. This leads to a nonlinear

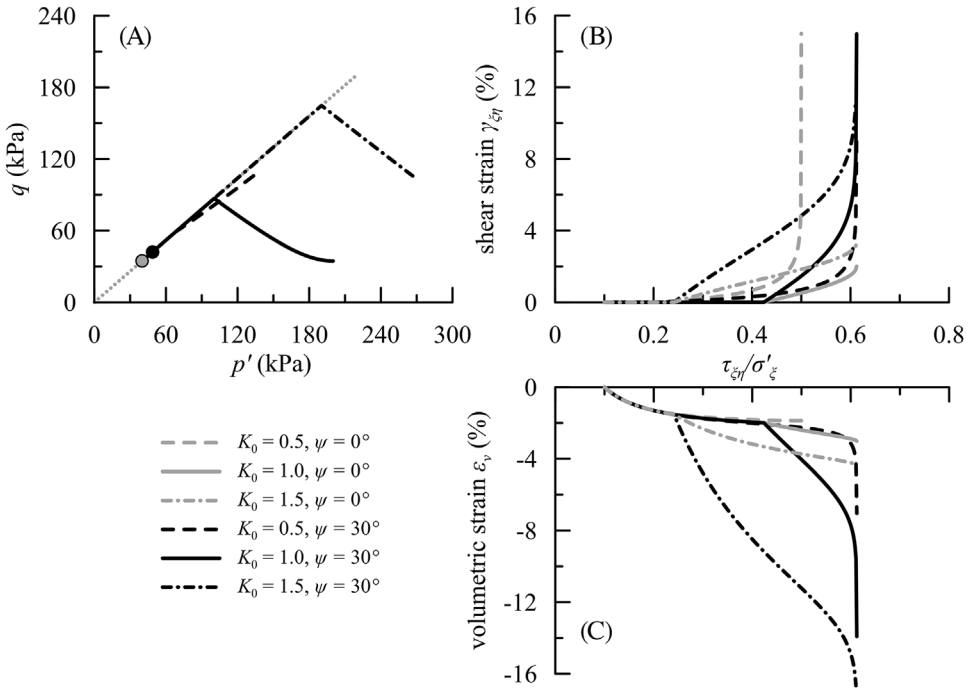

FIGURE 5 Simulations of simple shear response with decreasing normal effective stress and constant shear stress for different initial stress states and for associated and non-associated flow rule: (A) stress paths (dark curves) approaching the yield locus (dotted light gray line); (B) shear strain versus stress ratio; (C) volumetric strain versus stress ratio.

stress-strain response characterised by development of shear strains (Figure 5B) and curvature continuously increasing until the final state. Although the initial stress modifies the first yielding state, the final condition depends only on the dilation angle, with maximum strength occurring for the associated flow rule, analogously to what observed in the simple shear simulations. It is worth mentioning that in case of a non-associated flow rule and $K_0 \geq 1$, in analogy to what is observed in Figure 3, pseudo-softening would occur. Although the outcomes of this result cannot be reproduced with a stress-controlled simulation, they will later be discussed with reference to the dynamics of a landslide system undergoing changes in seasonal velocity, as relevant for the sliding-consolidation analyses conducted in this work.

Again, the nonlinear behaviour and the different first yielding conditions displayed in Figure 5 are a direct consequence of the multiaxial constitutive response. This is pointed out in Figure 6, where the results of the previous simulations obtained with a Drucker-Prager model under $K_0 = 0.5$ and $\psi = 30°$ are compared with those obtained with an interface-like frictional model of the MC type, expressed only in terms of normal and shear stress components, σ'_ξ and $\tau_{\xi\eta}$. If properly calibrated ($\varphi = 31.5°$ and $\psi = 30°$), the interface-like model leads to the same strength as that of the Drucker-Prager model, though characterised by a perfectly elasto-plastic behaviour, as shown with dotted lines in Figure 6. Conversely, when the complete 3D stress state is accounted for, first yielding is encountered at an earlier stage (point A) and the stress state evolves until reaching a final condition at point B. Afterwards, a new loading stage is applied to attain the original normal stress at point C, with the behaviour becoming purely elastic and volumetric strains being partially recovered. For subsequent loading-unloading cycles, the strain-stress curves of the Drucker-Prager and the interface-like models coincide, in that multiaxial effects disappear when the final condition is reached.

Although restricted to a material point and to a simple Drucker-Prager model without Lode angle dependence, the results above allow useful preliminary conclusions. Specifically, they demonstrate that a constitutive law based on 3D stress state gives rise to effects not accessible with standard frictional interface-like models, especially for newly activated landslides. By contrast, they show that the predictions of multiaxial constitutive laws do not differ substantially from those of interface-like models for landslide reactivation after dry periods, in that in these cases the landslide dynamics are controlled exclusively by changes in effective stress normal to the plane of sliding, but not by the stress components kinematically constrained by the system geometry (e.g., downslope and out of plane components).

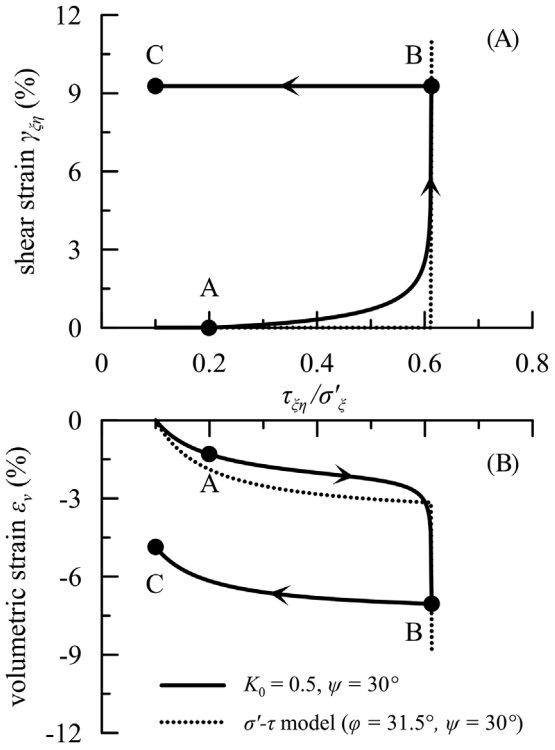

FIGURE 6 Drained simple shear test simulations of at constant shear stress: comparison between results between the Drucker-Prager model with 3D stress effects and the interface-like frictional model: (A) shear strain versus stress ratio; (B) volumetric strain versus stress ratio.

4 | PERFORMANCE OF THE AUGMENTED SLIDING CONSOLIDATION MODEL

In this section, the response of the proposed model is explored with reference to infinite slopes subjected to transient pore water pressure due to rainfall. The analyses build on the results of the previous section, in that it will be shown that hydrologic forcing gives rise to the same constitutive effects seen at material point level. In this case, however, it will be emphasised how these effects have crucial implications for the seasonal landslide motion arising from successive rainfall cycles.

The capabilities of the model are illustrated here with reference to the movement of landslide in California studied by Iverson and Major,[38] for which both pore water pressure and displacement data were reported. The dataset refers to the period from October 1982 to September 1985. The site is characterised by an average slope angle of 15°, with an estimated thickness of the landslide body and its basal shear zone of 6 and 1 m, respectively, while the groundwater level is located at 3.3 m depth ($h_w = 2.7$m). The parameters of the Drucker-Prager model and the hydraulic conductivity of the shear zone used to simulate the movement observed at this landslide site are reported in Table 1 (parameter Set 1).

The hydraulic conductivity, the soil unit weight and the strength parameters are consistent with those suggested by Iverson and Major,[38] while the values of the elastic moduli are appropriate for clay-rich formations.[39] The stress state has been initialised according to Equation (20) under K_0 conditions. In fact, since available information is insufficient to reconstruct the in situ stress state, here $K_0 = 1.0$ is assumed, corresponding to an over-consolidation ratio (OCR) of 3 according to Jaky's formula $K_0 = (1 - \sin\varphi)\mathrm{OCR}^{\sin\varphi}$. This choice of initial stress state can be considered viable for a shallow mechanism in clay soils. Moreover, it leads to an initial stress state lying within the elastic region of the model that justifies the stability condition of the slope before the application of the hydrologic forcing.

Figure 7A compares the pore water pressure change measured at the top of the shear band and the results of the numerical simulations obtained at the top and at the bottom of the shear zone. For numerical purposes, the pore pressure change due to seasonal rainfall has been simulated through a smooth interpolation of the data to reproduce the average variability of the pore pressure time series recorded at the site. The comparison between the monitored and calculated displacements shown in Figure 7B demonstrates that the model can capture the observed displacements trend over multiple cycles of rainfall if the parameters are properly calibrated.

Hereafter, idealised simulations are conducted with the goal of better illustrating how the evolution of the 3D effective stress state affects the landslide dynamics. The parameters chosen for the numerical simulations are inspired by well monitored landslides in clay-rich formations located in Northern California (e.g.,[38,40]). The landslide system considered hereafter is therefore modelled as an infinite slope with an inclination of 15° and initial water table and a shear band with thickness $h_s = 0.5$m located at 2 m depth. The parameters of the Drucker-Prager constitutive law with linear isotropic elasticity are those of the set 2 reported in Table 1, along with the hydraulic conductivity of the inelastic shear zone controlling the pore water pressure diffusion within the basal shear zone. Friction and dilatancy angles and the hydraulic conductivity are the key parameters of the model. The friction angle used for these illustrative analyses is higher than values usually reported for landslide reactivation (e.g.,[40]) and can thus be interpreted as an idealisation meant to replicate the deformation dynamics after first landslide initiation. Moreover, the combination of $\varphi = 30°$ and $\vartheta = 0°$ (pure shear condition) of the Drucker-Prager model corresponds to an equivalent friction angle, $\varphi_{eq} = 27°$, of the interface-like ($\sigma'_\xi - \tau_{\xi\eta}$) model.

TABLE 1 Model parameters.

Parameters	Set 1	Set 2	Units
γ_{sat}	21	19	kN/m^3
E	12700	12700	kPa
G	5000	5000	kPa
φ	21.4	30	°
θ	0	0	°
ψ	2	2	°
c	0	0	kPa
k	4.7×10^{-9}	5×10^{-10}	m/s
K_0	1.0	0.72, 1.0, 1.5	–

Note: γ_{sat}, saturated unit weight; φ, *friction angle;* ϑ, *Lode angle;* ψ, dilatancy angle; *c, cohesion;* E, Young's modulus; *G, shear modulus; k, hydraulic conductivity;* K_0, earth pressure coefficient at rest.

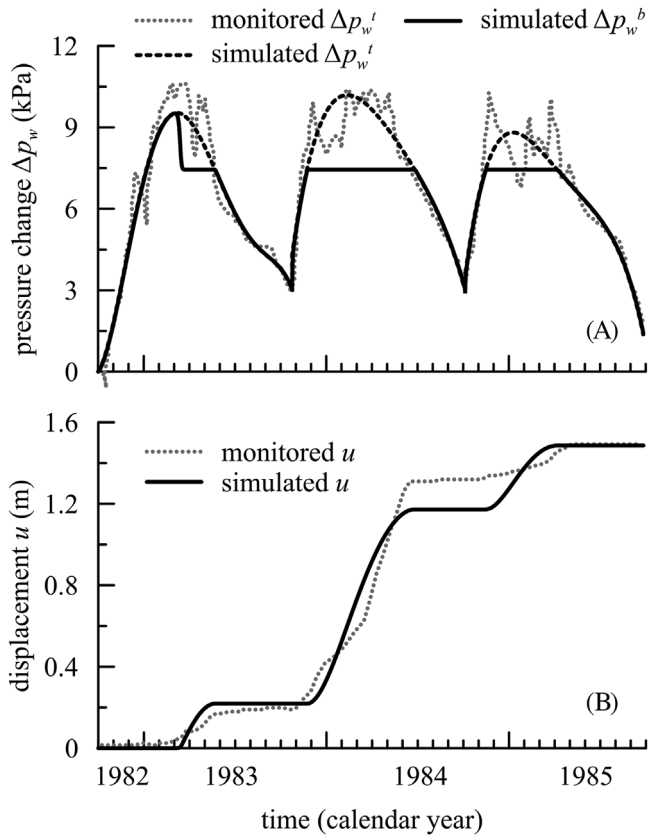

FIGURE 7 Simulations against monitored data for the Minor Creek landslide: (A) pore water pressure at the top and at the base of the shear zone and (B) cumulated displacements.

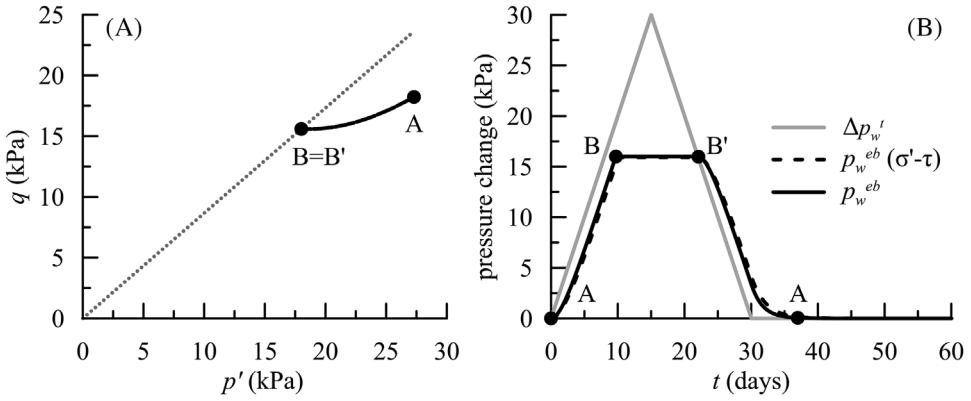

FIGURE 8 (A) stress path (solid line) at the base of the landslide due to the application of the input pore pressure (B) The dotted line represents the yield locus. The resulting pore water pressure at the base is shown for both 3D and interface-like formulations.

The initial stress state is evaluated according to Equation (20), considering three different values of $K_0 = 0.72,\ 1.0,\ 1.5$. The first value is chosen to replicate the same response as that of interface-like models, while the others aim at exploring the effect of stress states of over-consolidated soils, commonly observed in sloping ground. In fact, according to the Jaky's formula $K_0 = (1 - \sin\varphi)\mathrm{OCR}^{\sin\varphi}$, the values of $K_0 = 1.0,\ 1.5$ correspond to over-consolidation ratios (OCR) of 4 and 9, respectively. Since the determination of the in-situ stress state is characterised by a wide range of uncertainty, an inverse optimisation methodology might be used to set the value of K_0 that well fits with the field and laboratory observations. To reproduce the hydraulic forcing due to rainfall in a reasonable, though simplified way, a triangular pulse is used, as depicted in Figure 8B, where Δp_w^t denotes the input pore water pressure at the top of the shear band. The input pore pressure increases linearly with time until reaching its peak value and then goes back to zero for an extended period of

time. The maximum value of Δp_w^t is consistent with the pressure head fluctuations of about 3 m observed in situ in this type of translational landslides (e.g.,[38,40]).

Figure 8A shows the stress path in the p'-q plane obtained through the Drucker-Prager model, while Figure 8B shows the variation of the input pore water pressure with time as well as the excess pore water pressure p_w^{eb} at the base of the shear zone. The results in terms of basal pore water pressure show that the response within the shear zone is characterised by a delay with respect to the input until reaching complete dissipation. From the time corresponding to point A to that of point B the response is elastic, and the mean effective pressure decreases by virtue of the excess pore water pressure build-up. In correspondence to point B, the yield locus is reached, a steady-state condition in terms of stress is attained, with the basal pore pressure maintaining a constant value until the instant corresponding to point B'. Upon unloading, the material recovers its original stress state when the excess pore pressure is entirely dissipated. For the special case of $K_0 = 0.72$ and the choice of proper friction angles, the response of the multiaxial formulation coincides with that of the interface-like $(\sigma'_\xi - \tau_{\xi\eta})$ model, not only in terms of basal pore pressure, as illustrated in Figure 8B, but also with reference to the velocity and displacement fields in Figure 9. As long as the response is elastic, the slope is stable while when the elasto-plastic regime is engaged (point B) the sliding mechanism starts and permanent displacements, obtained by integration of the velocity field, accumulate until a purely elastic behaviour is recovered (point B').

The effect of the initial state of stress for the multiaxial formulation of the Drucker-Prager model is now explored. Figure 10 shows the stress paths in the p'-q plane, the shear strain against the ratio $\tau_{\xi\eta}/\sigma'_\xi$ and the displacements obtained after the triggering action of the top pore water pressure of Figure 8B for different initial stress states (points A_0, B_0 and D). It is worth noting the analogy with the constant shear stress simulations of Figures 5 and 6: The basal pore water pressure growth resulting from the coupled hydro-mechanical formulation leads to a reduction of the normal effective stress at constant $\tau_{\xi\eta}$ and consequently, in the first stage, the stress paths move towards the yield locus. When the yield surface is reached (yielding points A_y, B_y), the proposed formulation involves the evolution of the stress components σ'_η and σ'_χ until the steady state condition, characterised by the value of the earth coefficient K_0 in Equation (19) is attained. In light of this, it is clear that $K_0 = 0.72$ represents a very special case for the set of material parameters adopted here, in which the 3D effects are not engaged and the response coincides with that of the interface-like $(\sigma'_\xi - \tau_{\xi\eta})$ model. In fact, here the first yielding and the steady state condition coincide (point C) and this configuration holds as long as the hydraulic forcing is not removed. For any other initial conditions, the multiaxial formulation plays a role, and it manifests with an intensity that depends on the stress state prior to the hydrologic forcing. For example, in the cases of $K_0 = 1.0,\ 1.5$, when first yielding occurs the stress path moves along the yield surface until reaching point C in Figure 10A. The latter state can be interpreted as a steady state condition for the landslide system and, as expected, it is unique regardless of the initial stress state. As a result, it can be concluded that from points A_y and B_y to point C the stress state is evolving as a consequence of the 3D effects.

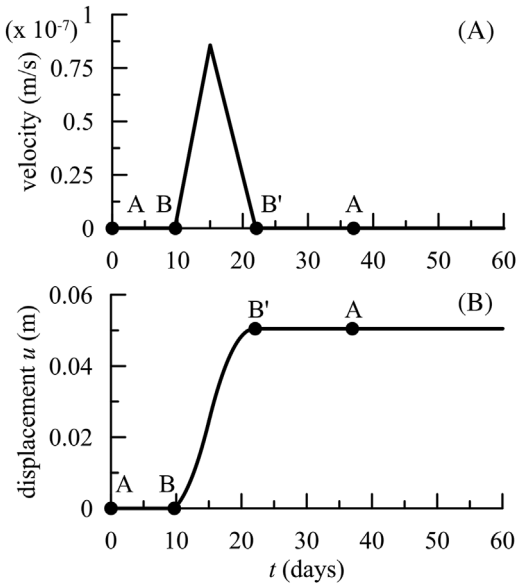

FIGURE 9 Velocity (A) and displacement (B) of the upper landslide mass triggered by the input pore pressure of Figure 7B.

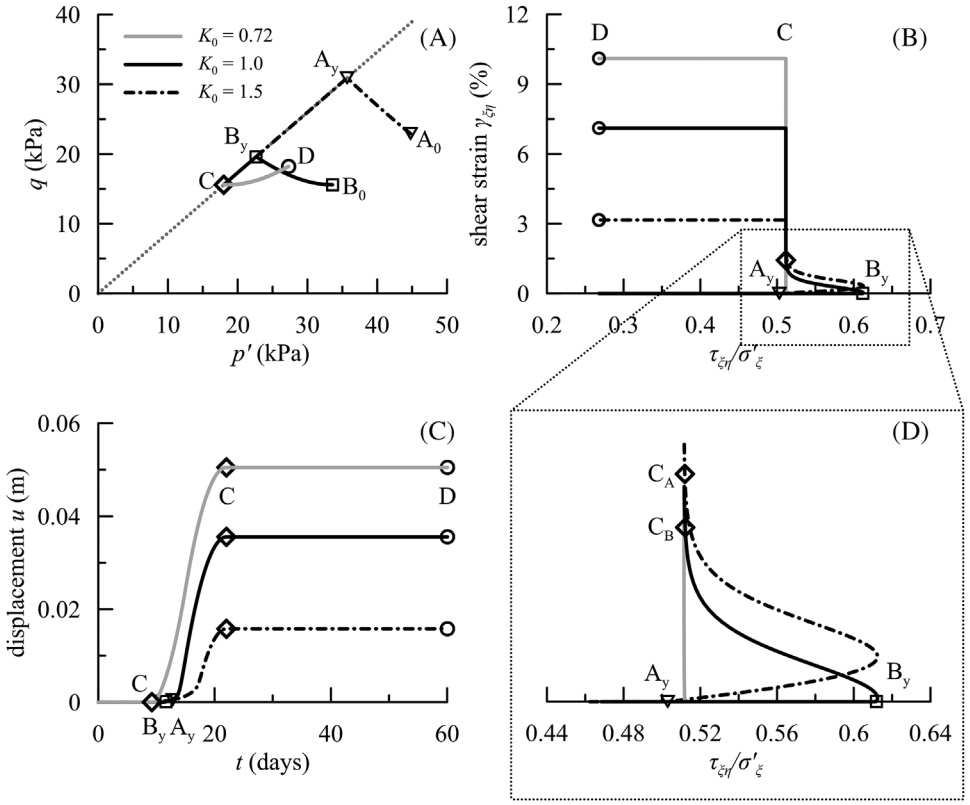

FIGURE 10 Effect of the initial stress state in terms of (A) stress path, (B) stress strain curves and (C) time displacements caused by the input pore pressure of Figure 7B. The stress paths move from points A_0, B_0 and D towards the yield surface represented by the dotted line, causing accumulation of shear strains and permanent displacement.

As shown in Figure 10B and D, the evolution of the stress state leads to an initial increase of the stress ratio $\tau_{\xi\eta}/\sigma'_\xi$, followed by its reduction until a steady state is reached. This pseudo-softening effect is not driven by specific constitutive assumptions, but rather by the evolution of the stress components σ'_η and σ'_χ, similar to what shown for the simulations of the reference element of volume in the previous section. Once the steady state condition is reached (point C), the multiaxial effects vanish and the formulation behaves identically to an interface-like model. The hydrologic forcing also leads to permanent displacements, as illustrated in Figure 10C, whose magnitude is significantly affected by the initial stress. In fact, the displacements occur earlier for decreasing values of K_0 as the distance from the initial stress state to the yield locus decreases. Although the multiaxial features disappear when the steady-state condition is reached, they produce some relevant and permanent effects on the response that are otherwise impossible to detect with a $\sigma'_\xi - \tau_{\xi\eta}$ formulation. Firstly, yielding is reached in correspondence to different stress states and at different times depending on the initial condition. Secondly, as the final stress state (point D) in Figure 10A is closer to the failure criterion than the initial states represented by the points A_0 and B_0, hydraulic forcing aggravates the stability conditions, as a new rainfall event of the same magnitude would produce greater displacements. Finally, the permanent shear strain accumulated by the end of a rainfall event is found to decrease as the initial value of K_0 increases. This is consistent with the fact that the more the soil is overconsolidated (and thus characterised by higher values of initial mean effective pressure at constant σ'_ξ), the higher is the basal pore pressure required to reach a steady state condition.

In the following, the response of the proposed model is explored when the basal shear zone of the landslide is subjected to cycles of pore water pressure input (Figure 11). The hydrologic input chosen for these simulations consists of 30 repeated cycles with maximum pore water pressure change of 20 kPa, for a total duration of 5 years.

Figure 12 illustrates the results of simulations characterised by initial stress states with $K_0 = 0.72$ and $K_0 = 1.5$ in terms of (a) stress paths in the meridian and (c) the deviatoric plane, (b) the evolution of displacements normalised with respect to the final values and (d) the evolution of the effective stress components σ'_ξ, σ'_η and σ'_χ with the number of hydraulic loading cycles depicted in Figure 11. In Figure 12 the initial states are denoted with the subscript 0, while y indicates first yielding. Similar to what was obtained for a single cycle of loading, the initial condition $K_0 = 0.72$ represents a special case

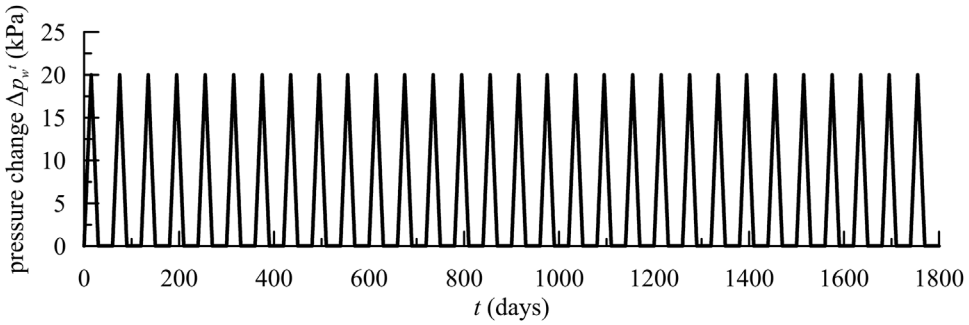

FIGURE 11 Input of pore water pressure consisting of 30 repeated cycles.

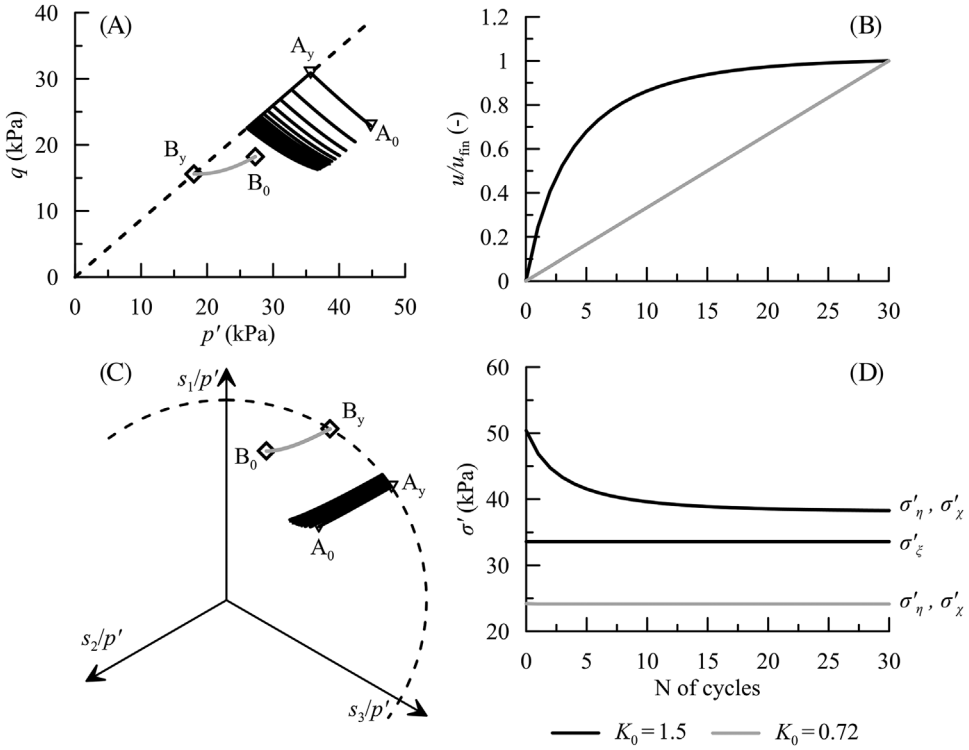

FIGURE 12 Results of the proposed model in response to cyclic pore pressure forcing ($\Delta p_w{}^t$=20 kPa) for different initial K_0 values. The stress paths in (A) and (C) move towards the dashed line representing the yield locus. The plot (D) shows the evolution of the downslope and out-of-plane stress components.

in which the multiaxial effects are silent, and the response coincides with that of the interface-like formulation. Therefore, the stress state upon yielding does not evolve and follows the same path for any cycles of the hydraulic forcing, while the displacement increases linearly with the number of cycles (Figure 12B) until a final value of 0.16 m. On the other hand, for the case of $K_0 = 1.5$ the stress path moves along the yield surface as the mean effective stress gradually decreases. This trend reflects the evolution of the downslope and out-of-plane stress components σ'_η and σ'_χ, whose values always coincide by virtue of the use of the DP model and decrease with the number of cycles until reaching a constant value (Figure 12D). The effective stress component σ'_ξ normal to the sliding surface does not change with the number of cycles as the total stress is constant and after each cycle the basal excess pore water pressure comes back to zero, like in Figure 8B. The modification of the effective stress state renders the constitutive response elastic after a few cycles and, as a result, the displacements stabilise to very small values (1 mm). This regime of response is here defined *shakedown* behaviour.

When the magnitude of the hydrologic forcing increases, the response is characterised by different regimes. To this purpose, Figure 13 illustrates the results of the simulation for the initial stress states with $K_0 = 1.5$ for the input pore water pressure at the top of the shear band shown in Figure 11 with peak values of 21 kPa. The first cycles, until the stress

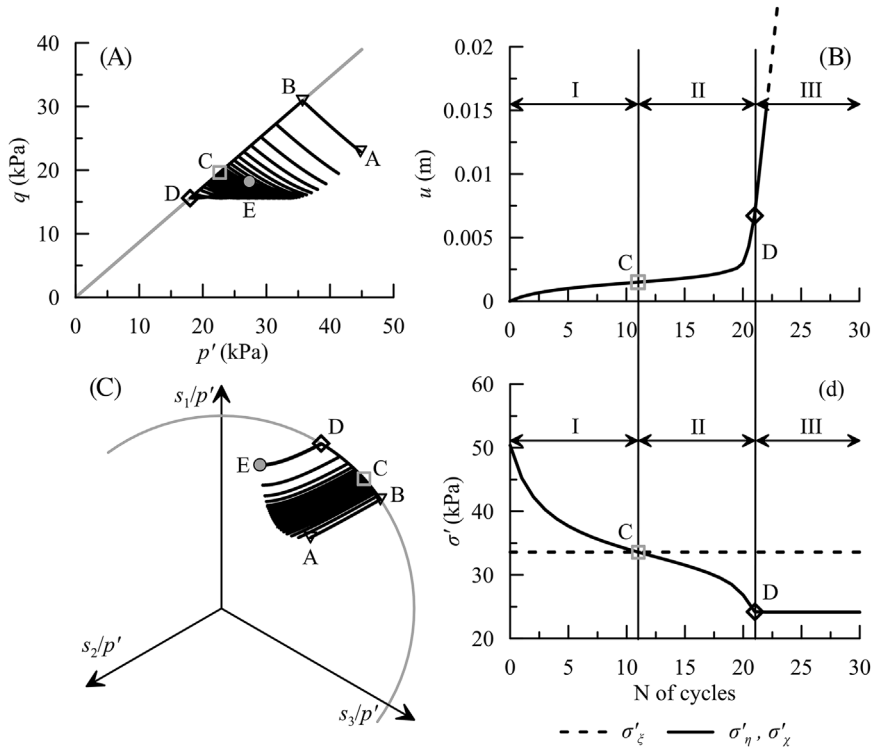

FIGURE 13 Results of the proposed landslide dynamics model in response to cycles of pore pressure ($\Delta p_w{}^t$=21 kPa) for initial $K_0 = 1.5$. Computed stress path at the base of the simulated landslide in the τ-σ' plane (A) and the π-plane (C). Evolution of landslide displacement (B) and normal effective stress components (D) with the number of cycles. The plots in (B) and (D) identify three regimes of response that are intimately related to the change of the downslope and out-of-plane effective stress components.

state reaches point C, identify a stage I characterised by a stabilisation of the permanent displacements with the number of cycles (Figure 13B), here denoted as *pseudo-shakedown*. In this first stage the values of the stress components σ'_η and σ'_χ decrease with the number of cycles and in correspondence of point C they equal the stress component σ'_ξ, that is constant throughout the loading process. The variation of these effective stress components is a natural consequence of the multiaxiality of the constitutive behaviour and continues until the steady state condition represented by point D is reached. During this process one can identify a stage II, associated to an increasing rate of accumulation of permanent displacements, called *short-lived cyclic failure*, in that it reflects the transient nature of this response. Finally, after point D is attained, the stress path follows the branch D-E under repeated cycles of loading and unloading (stage III) that characterise the final regime, in which the effective stress cartesian components along the chosen axes are constant, as well as the rate of displacements. Therefore, hereafter this stage will be referred to as *ratcheting*,[41–43] in that the multiaxial effects have vanished and the response of the model coincides with that typical of an interface-like behaviour (i.e., it involves no strength loss and linear growth of the displacements).

It is worth noting that in stage I, the term *pseudo-shakedown* is introduced to highlight the transient character of this regime and distinguish it from the proper *shakedown* behaviour shown in Figure 12. The presence of different regimes is a direct consequence of the 3D stress-strain formulation and cannot be recovered through an interface-like model. Therefore, stages I and II are transient and their manifestation depends on both the initial stress state and the magnitude/number of hydrologic loading cycles. The *shakedown* and *pseudo-shakedown* behaviours occur only for initial values of earth pressure coefficient $K_0 > 1$ and, as such, are relevant for moderately to highly over-consolidated soils. In these cases, the *pseudo-shakedown* is followed by a *short-lived cyclic failure* only if the rainfall is intense enough to overcome the threshold represented by the condition $K_0 = 1$. To better illustrate this point, Figure 14 shows the stress paths in the *p'-q* plane after the pore pressure input of Figure 11 for different magnitudes of p_w^t. In the case of Figure 14A, after few cycles, the stress path stops before reaching the point C as the behaviour becomes elastic. On the other side, when the amplitude Δp_w^t increases, not only *short-lived cyclic failure* occurs, but a smaller number of cycles is also required for *ratcheting* to take place. For each stress path, the evolution of displacements is also qualitatively illustrated.

Figure 15 shows in detail the evolution of slope displacement with the number of cycles for different values of pore water pressure at the top of the shear band and also illustrates the effects of progressive transition across regimes. Consistently with Figure 14A, for $\Delta p_w^t = 20$ kPa only the *shakedown* behaviour occurs and displacements increase until reaching a constant value, whereas for greater values of Δp_w^t the rate of displacements increases after stage I. For the sake of clarity, a semi-logarithmic plane is adopted in Figure 15A, in which one can identify the transition between *pseudo-shakedown* and

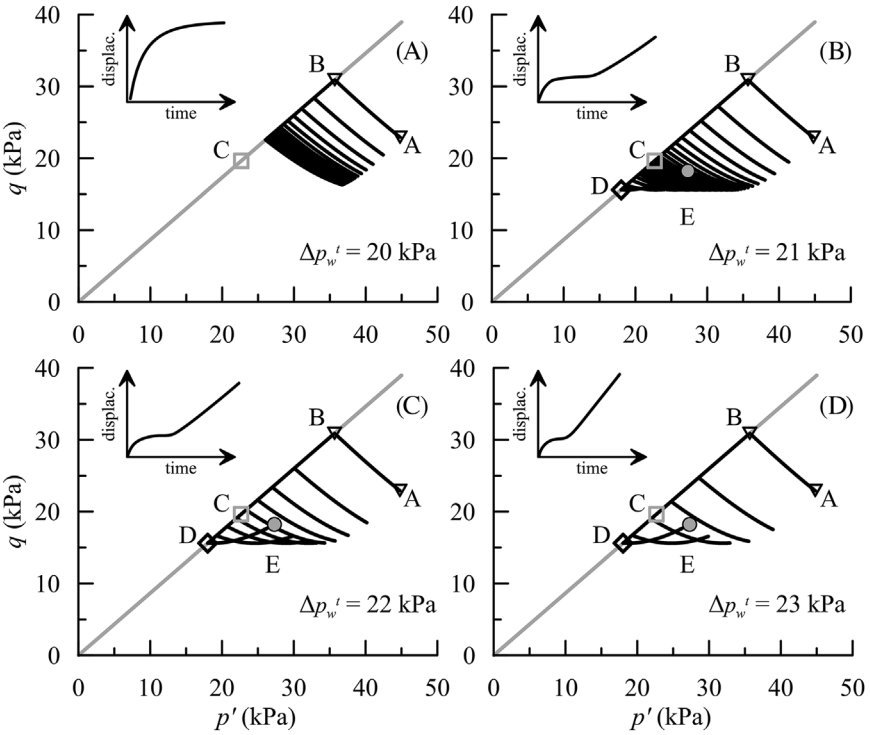

FIGURE 14 Stress paths computed for different amplitudes of pore pressure cycling (Figure 10). All stress paths start from point A and move towards the yield locus, depicted in greyscale. For increasing magnitude of hydrologic loading ($\Delta p_w{}^t$) the trend of displacements with time modifies as the different regimes of response are possibly engaged.

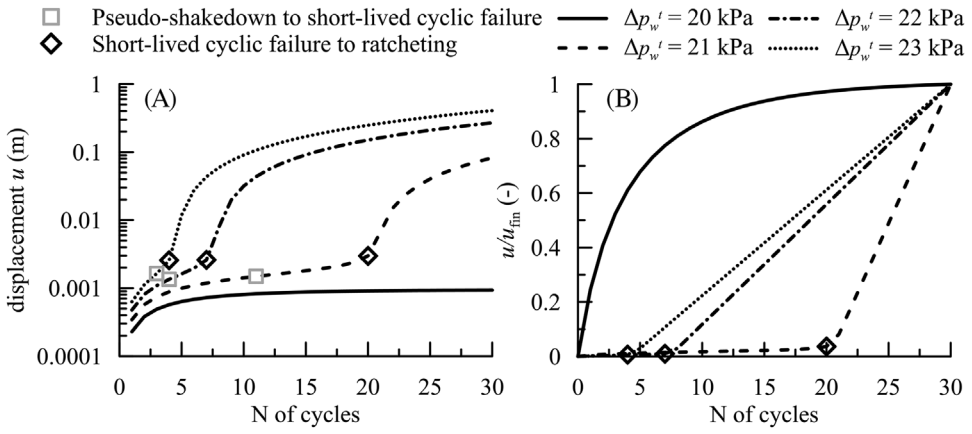

FIGURE 15 Evolution of (A) displacements and (B) normalised displacements with the number of cycles for different amplitudes of pore water pressure cycles ($\Delta p_w{}^t$).

short-lived cyclic failure in correspondence with the change of concavity of the curves and the entrance in the last regime with the sharp increase of displacements. In particular, the plot of the displacements normalised with respect to the final value in Figure 15B clearly shows the linear increase in values during *ratcheting* stage. It is, therefore, readily apparent that the higher the magnitude of the hydraulic forcing, the lower is the number of hydrologic cycles required to cause a transition from a regime to another. Moreover, during the last stage, the magnitude of the movement cumulated after each cycle depends only on the amplitude of Δp_w^t and hence, as expected, the final displacement increases for more severe and persistent rainfall events.

The results presented in Figures 14 and 15 suggest that the interface-like model can only reproduce satisfactorily the behaviour of landslides during the *ratcheting* regime but is not suitable for the complete description of the passage from initial mobilisation to the first phases of dynamic motion after a slope instability. In other words, it represents a useful and simple tool to characterise the steady state motion of a landslide that has been active for long period of times, for which the cumulation of new movements depends exclusively on the magnitude of the hydrologic forcing and its ability to alter the effective stress normal to the plane of sliding. However, recent landslides and newly formed mechanisms promoted by a

projected aggravation in climate may be subjected to hydrologic forcing never experienced before, thus producing trends of motion that are apparently stable in the early stages of their dynamics, but may eventually evolve into accelerating phenomena with potentially damaging consequences because of their large displacements and rates of motion.

5 | CONCLUSIONS

This paper presents a framework able to simulate the motion of hydrologically-driven landslides from the triggering to the propagation phase. Analytical approximations of the fields of excess pore pressure and velocity within the basal shear zone have enabled the governing equations to be condensed into a system of ODEs integrated at much lower computational cost compared to numerical methods for coupled hydro-mechanical problems (e.g., FEM, MPM, SPH). The most important feature of the framework is its ability to analyse the landslide dynamics with any inelastic constitutive law for the shear zone material, thus making it applicable for the study of landslide motion in any soil/rock type. At variance with previous models of this type, this study enables the role of the multi-dimensionality of the effective stress state within the landslide shear zone to be examined. This choice allowed for the first time, a comparison between the widely used description of the shear behaviour in terms of the stress-strain variables that directly reflect downslope sliding (in this paper referred to as *interface-like* models) with the response of a plastic continuum, in which the strain rate depends on the coupling of 3D stress components and kinematic constraints (e.g., plane strain conditions). As an outcome, it was possible to examine the effect of pseudo-hardening/softening previously documented in literature, but, to the authors' knowledge, never explored in a coupled hydro-mechanical context, where shear deformation is caused by pore water pressure developing and/or dissipating over time as a function of the hydro-mechanical properties of the geomaterials in which a landslide has formed.

The results have shown that, even in the presence of standard perfectly plastic frictional models with constant dependence on Lode angle, a 3D continuum formulation for the shear zone produces traits of landslide dynamics that cannot be captured by standard interface-like frictional laws. Notably, it was found that, if the motion of a landslide is simulated by treating the shear zone material as a plastic continuum, its dynamics become highly nonlinear, with the possibility of exhibiting transitions across different regimes of motion. Specifically, three regimes, all induced by hydrologic forcing, were identified: (i) a *pseudo-shakedown behaviour*, characterized by gradual adaptation, stable response, and no further motion after numerous cycles of forcing; (ii) a *short-lived cyclic failure* regime, characterised by temporary instability, with increasing landslide velocity with further forcing cycles until the last, defined as (iii) *ratcheting*, which emerges only after a large number of forcing cycles and involves constant seasonal velocity and fixed rates of displacement accumulation. Notably, it was found that perfectly plastic interface-like models enable only the simulation of regime (iii) but overlook regimes (i) and (ii), as well as the possibility of transitions across these types of motion. Furthermore, the analyses shown in this paper point out that the emergence of each regime and the transition from one to another is regulated by the evolution of effective stress components in constrained directions (i.e., downslope and out-of-plane normal effective stress). These effects are found to be governed by the in-situ stress (which in this study was reflected by the earth pressure coefficient at rest, K_0, prior to a rainfall event) and are predominant in regimes (i) and (ii). By contrast, it was found that multiaxial stress effects are silent, and thus negligible, during regime (iii), which in fact is the only type of landslide motion that can be replicated by interface-like models. In other words, while in regimes (i) and (ii) the downslope and out-of-plane stress components are influential in stabilising (regime [i]) or destabilising (regime [ii]) the landslide dynamics, during ratcheting (regime [iii]) the changes of effective stress normal to the plane of sliding (i.e., the only ones responding directly and solely to fluctuations of the pore pressure) are found to be the only cause of landslide movements and changes in seasonal velocity. Finally, the numerical simulations shown in this study suggest that for new and/or recently activated landslides, a transition across different regimes of motion is possible in response to an increase in the magnitude of hydrologic forcing. This finding emphasises that further research in the hydromechanics of landslides is particularly needed to evaluate the risks posed by projected changes in climate. From this standpoint, the benefits of the sliding consolidation framework proposed here are significant, in that it opens the way for a versatile choice of a site-specific geomaterial model and the incorporation of more reliable constitutive laws to understand and predict the long-term dynamics of landslides in hazard-prone regions.

ACKNOWLEDGEMENTS

The authors are grateful for the financial support provided by Leslie and Mac McQuown, which enabled the visit of F.R. at Northwestern University, during which this study was conducted. G.B. also gratefully acknowledges the financial support of the National Science Foundation, through grant ICER-1854951. Dr. Fabio Rollo acknowledges the RETURN Extended

Partnership and received funding from the European Union Next-GenerationEU (National Recovery and Resilience Plan—NRRP, Mission 4, Component 2, Investment 1.3 – D.D. 1243 2/8/2022, PE0000005). The authors are also grateful to Xiang Li, who participated to numerous discussions with the authors that expedited the simulations shown in this work, as well as to Angelo Amorosi, who facilitated their collaboration and provided useful input during the editing of the paper.

DATA AVAILABILITY STATEMENT

Data from the numerical analyses discussed in this paper can be made available to interested readers upon direct request to the authors.

ORCID

Fabio Rollo https://orcid.org/0000-0003-2526-8997
Giuseppe Buscarnera https://orcid.org/0000-0003-1664-9616

REFERENCES

1. Rianna G, Comegna L, Mercogliano P, Picarelli L. Potential effects of climate changes on soil–atmosphere interaction and landslide hazard. *Nat Hazards*. 2016;84(2):1487-1499.
2. Handwerger AL, Fielding EJ, Sangha SS, Bekaert DP. Landslide sensitivity and response to precipitation changes in wet and dry climates. *Geophys Res Lett*. 2022;49:e2022GL099499.
3. Gariano SL, Guzzetti F. Landslides in a changing climate. *Earth Sci Rev*. 2016;162:227-252.
4. Cascini L. Applicability of landslide susceptibility and hazard zoning at different scales. *Eng Geol*. 2008;102(3-4):164-177.
5. Hungr O, Leroueil S, Picarelli L. The Varnes classification of landslide types, an update. *Landslides*. 2014;11(2):167-194.
6. Lizárraga JJ, Frattini P, Crosta GB, Buscarnera G. Regional-scale modelling of shallow landslides with different initiation mechanisms: sliding versus liquefaction. *Eng Geol*. 2017;228:346-356.
7. Alonso EE, Gens A, Delahaye CH. Influence of rainfall on the deformation and stability of a slope in overconsolidated clays: a case study. *Hydrol J*. 2003;11(1):174-192.
8. Tommasi P, Boldini D, Caldarini G, Coli N. Influence of infiltration on the periodic re-activation of slow movements in an overconsolidated clay slope. *Can Geotech J*. 2013;50(1):54-67.
9. Pedone G, Ruggieri G, Trizzino R. Characterisation of climatic variables used to identify instability thresholds in clay slopes. *Geotech Lett*. 2018;8(3):231-239.
10. Borja RI, White JA, Liu X, Wu W. Factor of safety in a partially saturated slope inferred from hydro-mechanical continuum modeling. *Int J Numer Anal Methods Geomech*. 2012;36(2):236-248.
11. Elia G, Cotecchia F, Pedone G, et al. Numerical modelling of slope–vegetation–atmosphere interaction: an overview. *Q J Eng Geol Hydrogeol*. 2017;50(3):249-270.
12. Pedone G, Tsiampousi A, Cotecchia F, Zdravkovic L. Coupled hydro-mechanical modelling of soil–vegetation–atmosphere interaction in natural clay slopes. *Can Geotech J*. 2022;59(2):272-290.
13. Xu J, Ueda K, Uzuoka R. Numerical modeling of seepage and deformation of unsaturated slope subjected to post-earthquake rainfall. *Comput Geotech*. 2022;148:104791.
14. Bandara S, Ferrari A, Laloui L. Modelling landslides in unsaturated slopes subjected to rainfall infiltration using material point method. *Int J Numer Anal Methods Geomech*. 2016;40(9):1358-1380.
15. Ceccato F, Yerro A, Girardi V, Simonini P. Two-phase dynamic MPM formulation for unsaturated soil. *Comput Geotech*. 2021;129:103876.
16. Cuomo S, Di Perna A, Martinelli M. Modelling the spatio-temporal evolution of a rainfall-induced retrogressive landslide in an unsaturated slope. *Eng Geol*. 2021;294:106371.
17. Cascini L, Cuomo S, Pastor M, Rendina I. SPH-FDM propagation and pore water pressure modelling for debris flows in flume tests. *Eng Geol*. 2016;213:74-83.
18. Fávero Neto HA, Askarinejad A, Springman SM, Borja RI. Simulation of debris flow on an instrumented test slope using an updated Lagrangian continuum particle method. *Acta Geotech*. 2020;15(10):2757-2777.
19. Bui HH, Nguyen GD. Smoothed particle hydrodynamics (SPH) and its applications in geomechanics: from solid fracture to granular behaviour and multiphase flows in porous media. *Comput Geotech*. 2021;138:104315.
20. Hutchinson JN. A sliding–consolidation model for flow slides. *Can Geotech J*. 1986;23(2):115-126.
21. Pastor M, Quecedo M, Fernández Merodo JA, Herrores MI, Gonzalez E, Mira P. Modelling tailings dams and mine waste dumps failures. *Geotech*. 2002;52(8):579-591.
22. Pastor M, Martin Stickle M, Dutto P, et al. A viscoplastic approach to the behaviour of fluidized geomaterials with application to fast landslides. *Continuum Mech Thermodyn*. 2015;27:21-47.
23. Qiao SF, Clayton CRI. Flow slides run-out prediction using a sliding-consolidation model. *Landslides*. 2013;10(6):831-842.
24. Iverson RM. Regulation of landslide motion by dilatancy and pore pressure feedback. *J Geophys Res Earth Surf*. 2005;110(F2).
25. Chen Y, Buscarnera G. Unified modeling framework of flowslide triggering and runout. *Geotech*. 2022:1-14. doi:10.1680/jgeot.21.00370

26. Li X, Handwerger A, Buscarnera G, Dynamics of creeping landslides controlled by inelastic hydro-mechanical couplings. *Eng Geol*. 2023;317:107078
27. Pestana JM, Biscontin G, Nadim F, Andersen K. Modeling cyclic behavior of lightly overconsolidated clays in simple shear. *Soil Dyn Earthquake Eng*. 2000;19(7):501-519.
28. Drescher A, Detournay E. Limit load in translational failure mechanisms for associative and non-associative materials. *Geotech*. 1993;43(3):443-456.
29. Di Prisco C, Pisanò F. An exercise on slope stability and perfect elastoplasticity. *Geotech*. 2011;61(11):923-934.
30. Di Prisco C, Flessati L. Progressive failure in elastic–viscoplastic media: from theory to practice. *Geotech*. 2021;71(2):153-169.
31. Di Prisco C, Pastor M, Pisanò F. Shear wave propagation along infinite slopes: a theoretically based numerical study. *Int J Numer Anal Methods Geomech*. 2012;36(5):619-642.
32. Sloan SW, Abbo AJ. Biot consolidation analysis with automatic time stepping and error control Part 1: theory and implementation. *Int J Numer Anal Methods Geomech*. 1999;23(6):467-492.
33. Mihalache C, Buscarnera G. Diffusive instability of pore pressure transients in deformable unsaturated soils. *J Eng Mech*. 2016;142(11):04016091.
34. Coussy O. *Poromechanics*. John Wiley & Sons; 2004.
35. Wood DM. *Geotechnical Modelling*. CRC press; 2003.
36. Houlsby GT, Amorosi A, Rollo F. Non-linear anisotropic hyperelasticity for granular materials. *Comput Geotech*. 2019;115:103167. doi:10.1016/j.compgeo.2019.103167
37. Vermeer PA. The orientation of shear bands in biaxial tests. *Geotech*. 1990;40(2):223-236.
38. Iverson RM, Major JJ. Rainfall, ground-water flow, and seasonal movement at Minor Creek landslide, northwestern California: physical interpretation of empirical relations. *Geol Soc Am Bull*. 1987;99(4):579-594.
39. Obrzud R. *The Hardening Soil Model: A Practical Guidebook*. Zace Services; 2010.
40. Schulz WH, Smith JB, Wang G, Jiang Y, Roering JJ. Clayey landslide initiation and acceleration strongly modulated by soil swelling. *Geophys Res Lett*. 2018;45(4):1888-1896.
41. Postill H, Dixon N, Fowmes G, El-Hamalawi A, Take WA. Modelling seasonal ratcheting and progressive failure in clay slopes: a validation. *Can Geotech J*. 2020;57(9):1265-1279.
42. Postill H, Helm PR, Dixon N. Forecasting the long-term deterioration of a cut slope in high-plasticity clay using a numerical model. *Eng Geol*. 2021;280:105912.
43. Take WA, Bolton MD. Seasonal ratcheting and softening in clay slopes, leading to first-time failure. *Geotech*. 2011;61(9):757-769.

How to cite this article: Rollo F, Buscarnera G. Modelling seasonal landslide motion: Does it only depend on fluctuations in normal effective stress? *Int J Numer Anal Methods Geomech*. 2023;1-20. https://doi.org/10.1002/nag.3625